

Enhanced Whispering Gallery Mode Phase Shift using Indistinguishable Photon Pairs

Callum Jones,^{*} Antonio Vidiella-Barranco,[†] Jolly Xavier,[‡] and Frank Vollmer[§]
(Dated: April 29, 2024)

We present a theoretical investigation of a whispering gallery mode (WGM) resonator coupled to a Mach-Zehnder interferometer (MZI) and show a bimodal coincidence transmission spectrum when the input state is an indistinguishable photon pair. This is due to the doubled WGM phase shift experienced by the path-entangled state in the interferometer. Further, we model the noise in a WGM resonance shift measurement comparing photon pairs with a coherent state. At least a four-fold improvement in the signal-to-noise ratio (SNR) is possible, with clear implications for quantum-enhanced WGM sensing.

I. INTRODUCTION

Whispering gallery mode (WGM) resonators are optical cavities with a circular geometry which can take the form of ring resonators, toroids, spheres and bottles [1, 2]. These high-Q factor resonators have found many applications in sensing, including in biosensing, where plasmonic enhancements of the sensing signal using gold nanoparticles [3] have made it possible to detect single small molecules and enzyme turnover events, for example [4–7]. However, these sensors are far from reaching fundamental noise limits. Methods for improving the signal-to-noise ratio (SNR) have the potential to reveal more information from sensor signals such as detecting even smaller conformational changes in biomolecules.

Quantum sensing schemes with WGM sensors are as yet relatively unexplored. One widely used scheme in quantum optical sensing is the Mach-Zehnder interferometer (MZI) for determining an optical phase difference. With an indistinguishable photon pair as the input state, the state inside the interferometer is a two-photon N00N state due to Hong-Ou-Mandel (HOM) interference at the first beamsplitter. The phase shift between the two arms is doubled for the two-photon state and the interference fringes oscillate at double the frequency of the classical MZI, allowing these phase measurements to beat the quantum noise limit (QNL) [8]. This scheme has been demonstrated many times, including with higher order N00N states [9–11].

Typically, the quantum optical MZI has a linear phase difference introduced between the two arms. In this paper we investigate the behaviour of an MZI with a WGM resonance coupled to one of the interferometer

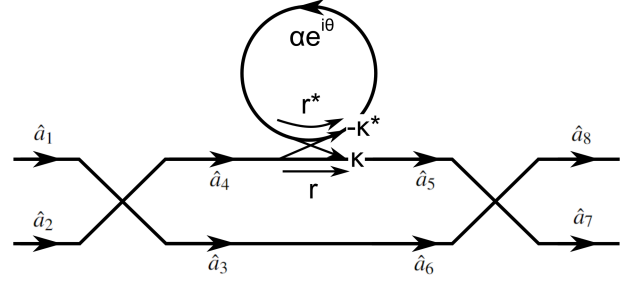


FIG. 1. Schematic of WGM resonator inside MZI.

arms, which introduces a phase shift and transmission profile dependent on the frequency detuning and coupling conditions. We use a model for quantum optical coupling to a WGM resonator based on the operator valued phasor addition (OVPA) model described in Ref. [12]. For an indistinguishable photon pair input state, we derive the output state analytically and show the WGM coincidence transmission spectrum has two dips, which is a consequence of doubling the WGM phase shift. We also demonstrate with a computational model how this spectral feature can enhance the SNR of a WGM resonance shift measurement, achieving at least a factor of 4 improvement in the SNR under reasonable experimental assumptions.

II. QUANTUM OPTICAL MODEL FOR WGM COUPLING

We use the OVPA approach described in Ref. [12] for a quantum optical treatment of coupling an optical mode in a waveguide to a ring resonator. In this model the waveguide-ring resonator system is parameterised as shown in Figure 1.

Coupling to the resonator (for example by evanescent coupling) is characterised by the amplitude coupling coefficient κ and amplitude reflection coefficient r , we use r to describe the coupling condition since $|\kappa|^2 + |r|^2 = 1$.

The mode in the ring resonator has an amplitude transmission α and phase θ per round trip. The intrinsic Q factor of the resonator is set by α . The phase θ is de-

^{*} c.jones20@exeter.ac.uk; Living Systems Institute, University of Exeter, Stocker Road, Exeter, EX4 4QD, UK

[†] Gleb Wataghin Institute of Physics - University of Campinas, 13083-859 Campinas, SP, Brazil

[‡] SeNSE, Indian Institute of Technology Delhi, Hauz Khas, New Delhi, India

[§] Living Systems Institute, University of Exeter, Stocker Road, Exeter, EX4 4QD, UK

pendent on the detuning δ between the frequency of the waveguide mode and a WGM, via $\theta = 2\pi Rn\delta/c$ where R is the resonator radius and n is the resonator refractive index. We consider detuning from a single WGM in the following.

The input-output relation for the waveguide mode coupled to the WGM resonator is:

$$\hat{a}_{out} = t(\omega)\hat{a}_{in} + \hat{F}(\omega). \quad (1)$$

This differs from the expression relating classical mode amplitudes by the extra term $\hat{F}(\omega)$ corresponding to noise operators. This must be included to satisfy the commutation relations for \hat{a}_{out} .

The complex amplitude transmission past the WGM resonator at frequency ω , $t(\omega)$, is:

$$t(\omega) = \left(\frac{r - \alpha e^{i\theta}}{1 - r^* \alpha e^{i\theta}} \right). \quad (2)$$

$T(\omega) = |t(\omega)|^2$ is the classical WGM transmission spectrum. The coupling condition may be varied through three regimes by changing r : $r > \alpha$ undercoupling, $r = \alpha$ critical coupling, and $r < \alpha$ overcoupling.

Noise operators $\hat{F}(\omega)$ couple the WGM to the bath of thermal modes in the environment around the resonator using a continuous set of beamsplitters to model losses, an approach due to Loudon [13]:

$$\hat{F}(\omega) = -i|\kappa|^2 \sqrt{\Gamma(\omega)} \sum_{n=0}^{\infty} (r^*)^n \times \int_0^{(n+1)L} dz \exp(i\xi(\omega)[(n+1)L - z]) \hat{s}(z, \omega) \quad (3)$$

where $\xi(\omega) = n(\omega)(\omega/c) + \Gamma(\omega)$ for ring resonator refractive index $n(\omega)$, and $\Gamma(\omega)$ is the loss per unit distance around the ring resonator. The continuous set of beamsplitters couple the modes $\hat{s}(z, \omega)$ to the WGM at position z on the ring, integrated up to the ring resonator circumference L .

III. WGM RESONATOR COUPLED TO MZI

Now we put the quantum optical model for the WGM resonator into a MZI as shown in Figure 1, such that it is coupled to one arm of the interferometer. The following sections investigate the consequences of this for coherent states and indistinguishable photon pairs at the MZI input modes.

A. Coherent State Input

First we consider the situation with quasi-classical light at the input to the MZI. If a coherent state with complex amplitude β is the input to mode \hat{a}_1 in the MZI, the amplitudes interfering on the second beamsplitter are

$\frac{1}{\sqrt{2}}\beta$ and $\frac{1}{\sqrt{2}}t(\omega)\beta$. The mode coupled to the WGM resonator experiences both a phase change and optical loss described by the transmission spectrum $t(\omega)$. The optical intensities at the output modes 7, 8 are then:

$$I_{7,8}(\omega) = \frac{1}{4} |(1 \pm t(\omega))\beta|^2 \quad (4)$$

The $I_7(\omega)$ spectrum has the form of a transmission dip similar to the transmission spectrum for a quasi-classical mode in a single waveguide coupled directly to a WGM resonance.

B. Indistinguishable Photon Pair Input

For the input state we take a simple expression for a photon pair at the input ports of the first beamsplitter:

$$|\psi_{in}\rangle = \hat{a}_1^\dagger \hat{a}_2^\dagger |0, 0\rangle_{1,2} \otimes |0\rangle_{env} \quad (5)$$

where $|0\rangle_{env}$ is the vacuum state for the environment, or a thermal bath of oscillators at temperature 0 K, which is acted on by the noise operators in the quantum WGM model. First we find the state in modes 5 and 6 after coupling to the WGM resonator.

Writing the relation between input (\hat{a}_1, \hat{a}_2) and output (\hat{a}_5, \hat{a}_6) modes in terms of a transfer matrix \mathbf{M} :

$$\begin{pmatrix} \hat{a}_5 \\ \hat{a}_6 \end{pmatrix} = \frac{1}{\sqrt{2}} \begin{pmatrix} it(\omega) & t(\omega) \\ 1 & i \end{pmatrix} \begin{pmatrix} \hat{a}_1 \\ \hat{a}_2 \end{pmatrix} + \begin{pmatrix} \hat{F}(\omega) \\ 0 \end{pmatrix} \quad (6)$$

$$\hat{\mathbf{a}}_{out} = \frac{1}{\sqrt{2}} \mathbf{M} \hat{\mathbf{a}}_{in} + \hat{\mathbf{F}}(\omega) \quad (7)$$

The output state in modes 5 and 6 after coupling to the WGM is given by substituting for $\hat{\mathbf{a}}_{in}^\dagger = (\hat{a}_1^\dagger, \hat{a}_2^\dagger)$ in the initial input state (Equation 5):

$$\begin{aligned} |\psi_{5,6}\rangle &= \frac{\sqrt{2}i}{2} \left(\frac{1}{(t^*(\omega))^2} A(\omega) |2, 0\rangle_{5,6} + |0, 2\rangle_{5,6} \right) \otimes |0\rangle_{env} \\ &\quad - \frac{i}{(t^*(\omega))^2} A(\omega) |1, 0\rangle_{5,6} \otimes \hat{F}^\dagger(\omega) |0\rangle_{env} \\ &\quad + \frac{i}{2(t^*(\omega))^2} A(\omega) |0, 0\rangle_{5,6} \otimes \hat{F}^{\dagger 2}(\omega) |0\rangle_{env}. \end{aligned} \quad (8)$$

$A(\omega)$ is a normalisation factor. The probability of the state $|0, 2\rangle_{5,6}$ should always be 1/2, so we normalise the other three terms with the parameter $A(\omega)$:

$$\begin{aligned} A^2(\omega) \left[\frac{1}{2|t(\omega)|^4} + \frac{1}{|t(\omega)|^4} |_{env} \langle 0 | \hat{F} \hat{F}^\dagger | 0 \rangle_{env} \right]^2 \\ + \frac{1}{4|t(\omega)|^4} |_{env} \langle 0 | \hat{F}^2 \hat{F}^{\dagger 2} | 0 \rangle_{env} \right]^2 = \frac{1}{2}. \end{aligned} \quad (9)$$

The expectation values of noise operators \hat{F} are evaluated using the commutation relation for the output mode amplitudes and using Equation 6, as described by Alsing et al. [12], leading to:

$$A(\omega) = |t(\omega)|^2 \left[1 + 2(1 - |t(\omega)|^2)^2 + 2(1 - |t(\omega)|^2)^4 \right]^{-1/2}. \quad (10)$$

As expected for the output state Equation 8, the

photon pairs in mode 6 have no dependence on the WGM coupling conditions, and the terms with photons in mode 5 have $A(\omega)/(t^*(\omega))^2$ dependence. This is where the double phase shift due to the two-photon N00N state comes in, because now due to the factor $(t^*(\omega))^2$ the phase difference between photons in modes 5 and 6 is twice the usual phase shift from coupling to a WGM resonator.

The next stage is to act on this state with the output beamsplitter to interfere modes 5 and 6 which have a phase difference equal to double the WGM phase shift. The final output state is:

$$|\psi_{out}\rangle = \frac{i\sqrt{2}}{4} \left(\frac{A(\omega)}{(t^*(\omega))^2} - 1 \right) |2,0\rangle_{7,8} \otimes |0\rangle_{env} + \frac{i\sqrt{2}}{4} \left(1 - \frac{A(\omega)}{(t^*(\omega))^2} \right) |0,2\rangle_{7,8} \otimes |0\rangle_{env} \\ + \frac{1}{2} \left(\frac{A(\omega)}{(t^*(\omega))^2} + 1 \right) |1,1\rangle_{7,8} \otimes |0\rangle_{env} - \frac{iA(\omega)}{\sqrt{2}(t^*(\omega))^2} |1,0\rangle_{7,8} \otimes \hat{F}^\dagger(\omega)|0\rangle_{env} \\ - \frac{A(\omega)}{\sqrt{2}(t^*(\omega))^2} |0,1\rangle_{7,8} \otimes \hat{F}^\dagger(\omega)|0\rangle_{env} + \frac{iA(\omega)}{2(t^*(\omega))^2} |0,0\rangle_{7,8} \otimes \hat{F}^{\dagger 2}(\omega)|0\rangle_{env}. \quad (11)$$

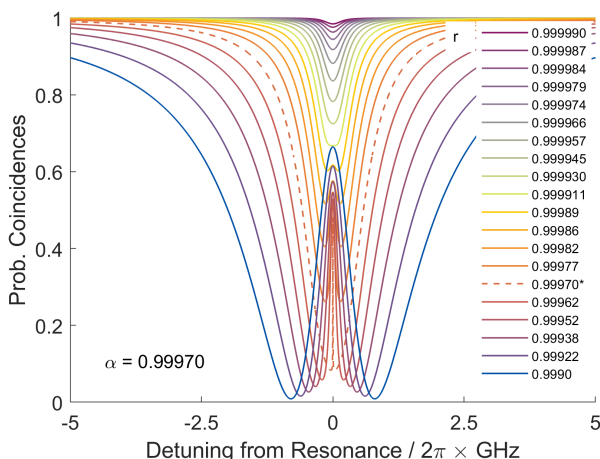


FIG. 2. Coincidence rate transmission spectra for indistinguishable photon pair input state to the WGM-coupled MZI. Coincidence probabilities are at the two MZI output modes. Spectra are shown for fixed round-trip transmission $\alpha = 0.9997$ and varying coupling coefficient r . Critical coupling ($r = \alpha$) is indicated by a dashed line.

Figure 2 shows the coincidence rate for $\alpha = 0.9997$ and varying coupling parameter r . This value of α gives a Q factor and linewidth γ typical of WGM sensing experiments ($\gamma \sim 100$ fm). Over a range of coupling conditions we can see that a double dip in the coincidence spectrum emerges as the coupling approaches critical coupling. This is in contrast to the typical Lorentzian dip in the classical WGM transmission spectrum.

As for the linear phase shift MZI, there are points

in the interference signal with a higher gradient and hence higher sensitivity to changes in the detuning, than in the classical WGM signal. In the next section we model WGM wavelength shift measurements with enhanced signal-to-noise ratio using these spectral features.

IV. MODELLING SIGNAL-TO-NOISE RATIO ENHANCEMENT FOR WGM MEASUREMENTS

In WGM sensing, changes in the resonance position and linewidth are tracked over time. We will now compare the noise in measurements of the WGM resonance shift between three measurement cases using coherent states and indistinguishable photon pairs.

A. Computational Model for Classical and Quantum WGM Sensing

We model three measurement cases:

1. ‘Classical WGM’ The transmission spectrum for a single mode coherent state (quasi-classical state) coupled to a WGM resonator, i.e. the ‘conventional’ WGM sensing experiment:

$$I_1(\omega) = |t(\omega)|^2. \quad (12)$$

2. ‘Classical WGM-MZI’ The transmission spectrum for a WGM resonator coupled to one arm of a MZI, with a coherent state in one input mode, and monitoring the transmission difference of the MZI outputs ($I_7 - I_8$ in

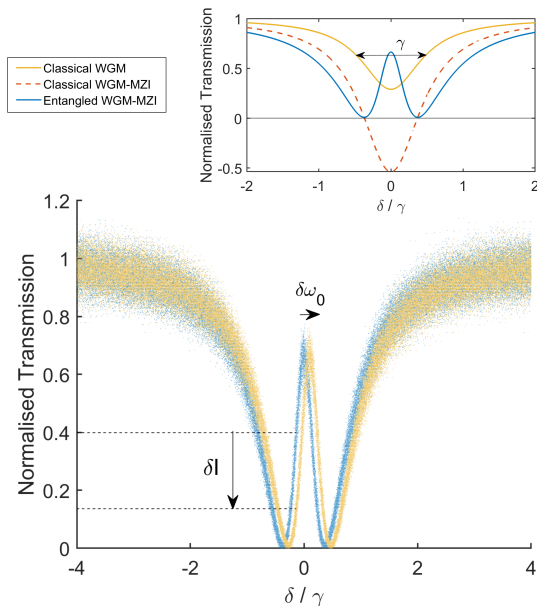


FIG. 3. Schematic of WGM measurement with noise for the entangled photon MZI case showing a resonance frequency shift transduced into an intensity change at the maximum gradient point in the spectrum. Detuning δ is in units of WGM linewidth γ . The top plot compares transmission spectra for the three cases introduced in the main text. The photon number per time bin was chosen to be $N = 380$ and a resonance frequency shift equal to 0.1γ . The resonator is in the overcoupled regime: $r = 0.9990$, $\alpha = 0.9997$.

Equation 4):

$$I_2(\omega) = \frac{1}{4} \left(|1 + t(\omega)|^2 - |1 - t(\omega)|^2 \right). \quad (13)$$

3. ‘Entangled WGM-MZI’ The transmission spectrum for a WGM resonator coupled to one arm of a MZI, with indistinguishable photon pairs in the two input modes, and measuring coincidence detections in the two output modes:

$$P_{Coinc}(\omega) = \frac{1}{4} \left| \frac{A(\omega)}{(t^*(\omega))^2} + 1 \right|^2. \quad (14)$$

The change we would like to detect for sensing experiments is a shift in the WGM resonance frequency $\delta\omega_0$. We consider a transmission intensity measurement at a single point where the transmission spectrum has maximum gradient, i.e. at fixed detuning from resonance. From the transmission measurement we read out both changes in linewidth γ and resonance position ω_0 as a combined frequency change $\Omega = \delta\omega_0 + 0.5(\delta\gamma)$.

For each of the three cases introduced above, we add randomly generated noise to the intensity and resonance position of the model signal, as shown in Figure 3. In each simulation, spectra were generated for $N_{steps} = 10^3$ time steps. For each time step, two types of noise were

added to the transmission spectrum: a Gaussian distributed change in the resonance frequency ω_0 (to model noise sources affecting the WGM resonator such as thermorefractive noise, changes in the coupling conditions, or fluctuations in the laser wavelength), and Poisson distributed noise in the measured transmission intensity (photon shot noise due to counting small numbers of photons per time bin). The dimensionless photon number per time bin N is normalised for equal $\langle N \rangle$ at the WGM resonator, see Supplementary Information (SI).

B. Modelling Results

Figure 4(a) shows the 3σ uncertainty $\Delta\Omega$ for classical WGM, classical WGM-MZI, and entangled WGM-MZI as a function of detected photon number per time bin (N is the number of coincidences per time bin for the photon pair case). The coupling conditions are set to slightly overcoupled: $\alpha = 0.9997$ and $r = 0.9996$. The combined frequency change Ω is given in wavelength units for comparison to experimental results with WGM sensing. The 1σ level of noise added to the resonance wavelength was 1 fm which was chosen to be near typical experimental values [7, 14].

There are two main regimes: for photon number $N > 10^5$, the resonance frequency noise dominates and the noise is constant as the optical power increases, 3 fm expected from the $1\sigma = 1$ fm noise which was added. This is the regime in which typical WGM sensing experiments will operate. For $N < 10^4$, shot noise begins to dominate and the uncertainty in the wavelength shift increases as \sqrt{N} as the number of photons per time bin N decreases. In this regime, we see that the entangled WGM-MZI has reduced noise in the wavelength shift compared to the two classical cases.

Figures 4(b,c) show maps of the relative noise comparing the entangled WGM-MZI case with (a) classical WGM and (b) classical WGM-MZI. The plotted noise ratio values are the enhancement factor of the SNR, compared to the classical SNR. Here $N = 380$; at the upper end of the shot-noise limited regime in Figure 4(a). For (b) and (c) the SNR enhancement is consistently higher in the overcoupling region and has a peak at the critical coupling condition.

We also consider the effect of the input light linewidth, which so far has been assumed to be monochromatic. To model this effect, the transmission spectra for each case were convolved with a Gaussian function. Figure 5 shows the entangled WGM-MZI noise level relative to the classical WGM case, including the linewidth of the input light. This is a slice through Figure 4(c) shown by the horizontal line.

The ratio between the input linewidth and the WGM linewidth (the linewidth of the classical WGM spectrum) was varied between 0.1 and 1.0. For an experimentally achievable ratio 0.1 [15], the SNR enhancement is up to a factor of 4. For an input linewidth equal to the WGM

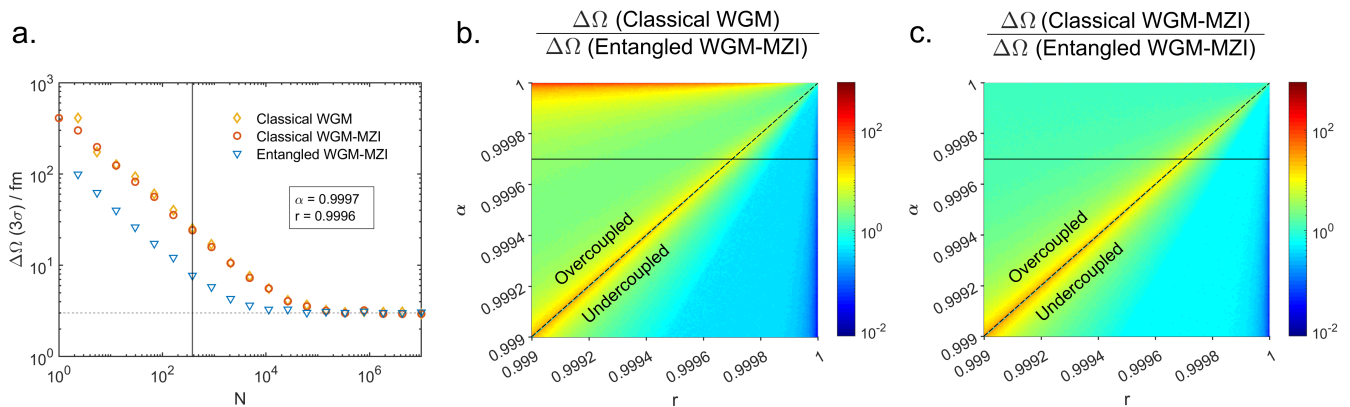


FIG. 4. (a) Noise (3σ) in the WGM wavelength shift against photon number per time bin N at fixed $r = 0.9996$ (overcoupling). (b) SNR enhancement factor for entangled WGM-MZI relative to classical WGM case as a function of WGM parameters r and α . (c) SNR enhancement for entangled WGM-MZI relative to the classical WGM-MZI case. Fixed photon number per time bin $N = 380$.

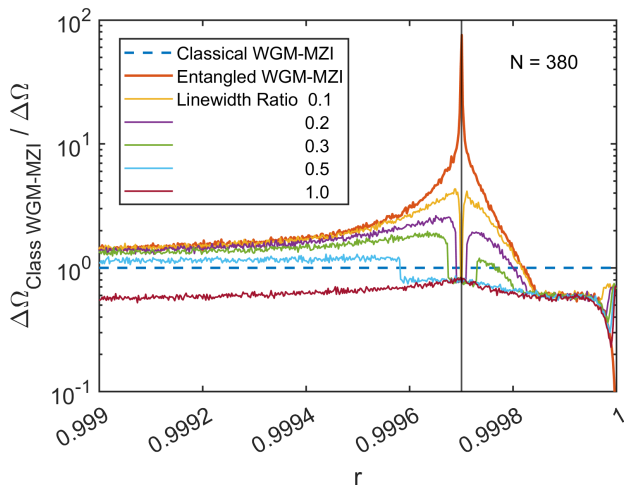


FIG. 5. SNR enhancement factor for WGM wavelength shift relative to classical WGM-MZI case, plotted against coupling parameter r at fixed photon number per time bin $N = 380$. Lines show the entangled WGM-MZI SNR enhancement when the input photon pair spectral width is 0.1, 0.2, 0.3, 0.5, and 1.0 times the WGM linewidth.

linewidth, there is no sensitivity enhancement.

The large peak in the SNR enhancement around critical coupling is not only strongly dependent on the input state spectral width but also corresponds to the central peak of the coincidence spectrum becoming vanishingly narrow at $r = \alpha$. Therefore the dynamic range for sensing resonance wavelength shifts is very low near critical coupling, see SI. The most robust SNR advantage is obtained in the overcoupled regime, where there is an enhancement of at least a factor of 4 (for linewidth ratio 0.1).

V. DISCUSSION: RELEVANCE TO WGM SENSING

A SNR enhancement in measurements of the WGM resonance shift promises to improve the performance of WGM sensors which are applied to precise measurements in, e.g., temperature [16–18], pressure [19, 20], and biosensing [3, 4] including single molecule detection when combined with optoplasmonic enhancements [5, 6, 21]. Here we showed an advantage to using indistinguishable photon pairs in the shot noise limited sensing regime, with an achievable factor of 4 enhancement in the SNR, taking into account the photon spectral width.

In summary, conditions for the optimum enhancement are: *i.* the measurement is in the shot noise-limited regime, *ii.* the WGM resonator is overcoupled, and *iii.* the input photon pair state is spectrally narrow: ~ 0.1 times the WGM linewidth. See SI for further discussion of how this experiment can be realised.

To achieve practical enhancements to WGM sensing in areas such as single molecule detection, we would need to work at an optical power comparable to current classical measurements ($\sim \mu\text{W}$ - mW). Could squeezed states also offer a SNR enhancement in WGM measurements with higher optical power? Recent theoretical studies by Belsley et al. call this into question [22]. It will be important to consider whether squeezing provides any advantage subject to the experimental constraints for particular WGM sensing methods, and for experiments using two optical modes as we studied here.

ACKNOWLEDGMENTS

The authors would like to thank Professor José A. Roversi and Dr Charles Downing for valuable discussions about the results and manuscript.

C.J. would like to thank Dr Lucia Caspani and Dr Isaac Luxmoore for their feedback on an early version of this manuscript, and Dr Jesús Rubio for advice about quantum metrology.

C.J. and F.V. thank support from the Engineering and Physical Sciences Research Council (EPSRC), under grants EP/X018822/1 and EP/R031428/1.

A.V.-B. would like to thank the Air Force Office of Scientific Research (AFOSR), USA, under award N° FA9550-24-1-0009, and Conselho Nacional de Desenvolvimento Científico e Tecnológico, (CNPq), Brazil, via the Instituto Nacional de Ciência e Tecnologia - Informação Quântica (INCT-IQ), grant N° 465469/2014-0.

-
- [1] X. Jiang, A. J. Qavi, S. H. Huang, and L. Yang, Whispering-gallery sensors, *Matter* **3**, 371 (2020).
- [2] D. Yu, M. Humar, K. Meserve, R. C. Bailey, S. N. Chormaic, and F. Vollmer, Whispering-gallery-mode sensors for biological and physical sensing, *Nat Rev Methods Primers* **1**, 10.1038/s43586-021-00079-2 (2021).
- [3] M. A. Santiago-Cordoba, S. V. Boriskina, F. Vollmer, and M. C. Demirel, Nanoparticle-based protein detection by optical shift of a resonant microcavity, *Applied Physics Letters* **99**, 073701 (2011), <https://pubs.aip.org/aip/apl/article-pdf/doi/10.1063/1.3599706/14455952/073701.1.online.pdf>.
- [4] L. He, Şahin Kaya Özdemir, J. Zhu, W. Kim, and L. Yang, Detecting single viruses and nanoparticles using whispering gallery microlasers, *Nature Nanotech* **6**, 428 (2011).
- [5] M. Baaske and F. Vollmer, Optical observation of single atomic ions interacting with plasmonic nanorods in aqueous solution, *Nature Photon* **10**, 733 (2016).
- [6] S. Vincent, S. Subramanian, and F. Vollmer, Optoplasmonic characterisation of reversible disulfide interactions at single thiol sites in the attomolar regime, *Nat Commun* **11**, 10.1038/s41467-020-15822-8 (2020).
- [7] S. Subramanian, H. B. Jones, S. Frustaci, S. Winter, M. W. van der Kamp, V. L. Arcus, C. R. Pudney, and F. Vollmer, Sensing enzyme activation heat capacity at the single-molecule level using gold-nanorod-based optical whispering gallery modes, *ACS Applied Nano Materials* **4**, 4576 (2021).
- [8] J. P. Dowling, Quantum optical metrology – the low-down on high-N00N states, *Contemporary Physics* **49**, 125 (2008).
- [9] T. Nagata, R. Okamoto, J. L. O’Brien, K. Sasaki, and S. Takeuchi, Beating the standard quantum limit with four-entangled photons, *Science* **316**, 726 (2007), <https://www.science.org/doi/pdf/10.1126/science.1138007>.
- [10] A. Crespi, M. Lobino, J. C. F. Matthews, A. Politi, C. R. Neal, R. Ramponi, R. Osellame, and J. L. O’Brien, Measuring protein concentration with entangled photons, *Applied Physics Letters* **100**, 233704 (2012), <https://pubs.aip.org/aip/apl/article-pdf/doi/10.1063/1.4724105/14251724/233704.1.online.pdf>.
- [11] S. Slussarenko, M. M. Weston, H. M. Chrzanowski, L. K. Shalm, V. B. Verma, S. W. Nam, and G. J. Pryde, Unconditional violation of the shot-noise limit in photonic quantum metrology, *Nature Photon* **11**, 700 (2017).
- [12] P. M. Alsing, E. E. Hach, C. C. Tison, and A. M. Smith, Quantum-optical description of losses in ring resonators based on field-operator transformations, *Phys. Rev. A* **95**, 053828 (2017).
- [13] R. Loudon, *Quantum Theory of Light*, 3rd ed. (Oxford University Press, 2000).
- [14] S. Subramanian, S. Vincent, and F. Vollmer, Effective linewidth shifts in single-molecule detection using optical whispering gallery modes, *Applied Physics Letters* **117**, 151106 (2020), <https://pubs.aip.org/aip/apl/article-pdf/doi/10.1063/5.0028113/14539442/151106.1.online.pdf>.
- [15] F. Wolfgramm, Y. A. de Icaza Astiz, F. A. Beduini, A. Cerè, and M. W. Mitchell, Atom-resonant heralded single photons by interaction-free measurement, *Phys. Rev. Lett.* **106**, 053602 (2011).
- [16] Y.-Z. Yan, C.-L. Zou, S.-B. Yan, F.-W. Sun, Z. Ji, J. Liu, Y.-G. Zhang, L. Wang, C.-Y. Xue, W.-D. Zhang, Z.-F. Han, and J.-J. Xiong, Packaged silica microsphere-taper coupling system for robust thermal sensing application, *Opt. Express* **19**, 5753 (2011).
- [17] X. Xu, X. Jiang, G. Zhao, and L. Yang, Phone-sized whispering-gallery microresonator sensing system, *Opt. Express* **24**, 25905 (2016).
- [18] R. Luo, H. Jiang, H. Liang, Y. Chen, and Q. Lin, Self-referenced temperature sensing with a lithium niobate microdisk resonator, *Opt. Lett.* **42**, 1281 (2017).
- [19] A. Bianchetti, A. Federico, S. Vincent, S. Subramanian, and F. Vollmer, Refractometry-based air pressure sensing using glass microspheres as high-Q whispering-gallery mode microresonators, *Optics Communications* **394**, 152 (2017).
- [20] S. Basiri-Esfahani, A. Armin, S. Forstner, and W. P. Bowen, Precision ultrasound sensing on a chip, *Nature Communications* **10**, 10.1038/s41467-018-08038-4 (2019).
- [21] E. Kim, M. D. Baaske, I. Schuldes, P. S. Wilsch, and F. Vollmer, Label-free optical detection of single enzyme-reactant reactions and associated conformational changes, *Science Advances* **3**, e1603044 (2017).
- [22] A. Belsley, E. J. Allen, A. Datta, and J. C. F. Matthews, Advantage of coherent states in ring resonators over any quantum probe single-pass absorption estimation strategy, *Phys. Rev. Lett.* **128**, 230501 (2022).
- [23] A. Fedrizzi, T. Herbst, A. Poppe, T. Jennewein, and A. Zeilinger, A wavelength-tunable fiber-coupled source of narrowband entangled photons, *Opt. Express* **15**, 15377 (2007).
- [24] S. M. Lee, H. Kim, M. Cha, and H. S. Moon, Polarization-entangled photon-pair source obtained via type-II non-collinear SPDC process with PPKTP crystal, *Opt. Express* **24**, 2941 (2016).
- [25] J. Fekete, D. Rieländer, M. Cristiani, and H. de Riedmatten, Ultranarrow-band photon-pair source compatible with solid state quantum memories and telecommunication networks, *Phys. Rev. Lett.* **110**, 220502 (2013).
- [26] J. V. Rakonjac, S. Grandi, S. Wengerowsky, D. Lago-Rivera, F. Appas, and H. de Riedmatten, Transmission of light-matter entanglement over a metropolitan network,

Appendix A: Relating the WGM Model to Typical Experimental Parameters

In sensing experiments, it is more typical to characterise a WGM resonator and coupling conditions using its linewidth in wavelength units $\Delta\lambda$ and its Q factor. The dimensionless parameters α, r can be related to these quantities through the following expressions.

$$\Delta\lambda = -\frac{\lambda_o^2 \ln(|\alpha r|)}{4\pi^2 R} \quad (\text{A1})$$

$$Q = \frac{\lambda_o}{\Delta\lambda} = -\frac{4\pi^2 R}{\lambda_o \ln(|\alpha r|)}. \quad (\text{A2})$$

The WGM resonator radius is R and the resonance wavelength λ_o .

Appendix B: Experimental Considerations

To realise this experiment, we require a source of indistinguishable photon pairs showing high HOM interference visibility (e.g. from SPDC in a nonlinear crystal such as PPKTP [23, 24]).

The setup might be built with an all-fibre MZI, using a tapered optical fibre to couple photons to e.g. a microsphere, or alternatively by fabricating the MZI with integrated photonics and using a microring resonator. In either case, the wavelength of the photon pairs must be tuneable in order to match the wavelength of WGM, with fine tuning to enable scanning across the WGM spectrum. To observe the SNR enhancement, the photon pairs must be spectrally narrow: ideally at least ~ 0.1 of the WGM linewidth (typically ~ 100 MHz for WGM microsphere sensors).

To meet all of these requirements, photon pairs generated by cavity-assisted SPDC seem the most promising, which is a technique already being used for coupling entangled photons to atomic transitions [15, 25] (typically for quantum memories [26]). Refs. [15, 25] report photon pair bandwidths of 7 MHz and 2 MHz, respectively, therefore a bandwidth of < 0.1 of the WGM linewidth is realistic.

Appendix C: Comparing Photon Number Resources for each Measurement Case

1. Normalising Photon Rates

For a fair comparison between measurement cases, the average photon number resources $\langle N \rangle$ reaching the WGM resonator should be equal in all three cases. Table SI

Measurement Case	Input Rate	WGM Rate	Detection Rate
Classical WGM	R	$R = P$	R
Classical WGM-MZI	$2R$	$R = P$	$2R$
Entangled WGM-MZI	P^*	P	P^*

TABLE I. **Photon rates in three measurement cases.** WGM rate refers to the photon rate in the waveguide coupled to the WGM resonator. Detection rates are the maximum detection rates which would be measured far from resonance. Entries marked * are coincidence rates.

summarises the photon rates at the input, the photon rate in the mode coupled to the WGM, and the detected photon rate.

We consider first an input photon pair coincidence rate P for the entangled WGM-MZI case. The mean single photon rate before the WGM is also P , then the maximum (off-resonance) detected coincidence rate is P .

For the classical WGM-MZI case, we set the photon rate in the mode before the WGM to be $R = P$. To give this rate, the photon rate at one input of the MZI must be $2R$. The maximum detected photon rate at both outputs is then $2R$. This maximum rate corresponds to the rate measured by a transmission difference measurement across the two outputs when off resonance.

Finally, for the classical WGM case there is only one waveguide so the input, WGM, and maximum detected rates are all set to be R .

Therefore, the maximum detected photon rate in the classical WGM case and the maximum coincidence rate in the entangled case are equal: $R = P$. The maximum detected rate for the classical WGM-MZI transmission difference measurement is $2R$. A photon number per time bin N was used to calculate the shot noise level in the classical WGM and entangled WGM-MZI cases, and $2N$ in the classical WGM-MZI case.

2. Measurement on Classical WGM-MZI

We cannot make exactly the same measurement on the classical WGM-MZI setup as with the entangled WGM-MZI setup since the entangled case uses a coincidence measurement on the photon pairs. The two outputs of the classical WGM-MZI have transmission signals corresponding to a dip and peak, respectively. We considered both transmission measurements on a single output (with the transmission dip) and on both outputs by taking the difference ($I_7 - I_8$ from Equation 4 in the main text).

Figure 6 compares the results for the noise in resonance shift $\Delta\Omega$. The difference measurement slightly reduces the noise in the shot noise limited regime for the classical WGM-MZI case compared with a single mode measurement. Therefore, we use this difference measurement for all comparisons in the main text.

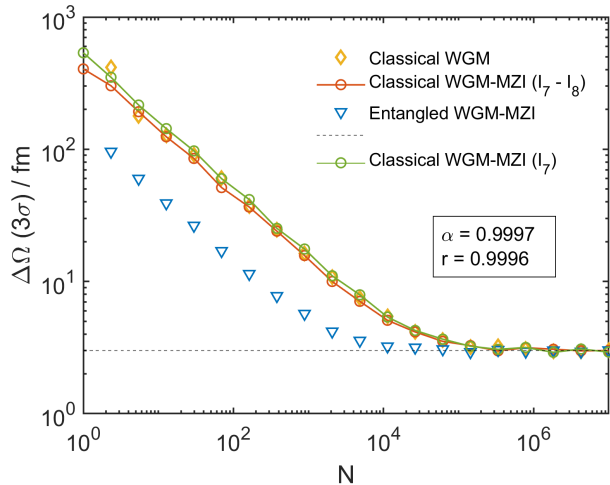


FIG. 6. Comparing single output and difference measurements for classical WGM-MZI case. Noise (3σ) in the WGM wavelength shift against photon number per time bin N at fixed $r = 0.9996$ (overcoupling). Orange (green) lines show the noise level for the classical WGM-MZI transmission difference (single output) measurement, demonstrating the difference measurement has slightly lower noise in the shot noise limited regime and reaches the same limit in the high N regime.

Appendix D: Additional Plots from Computational Model

Figure 7 shows the resonance position noise $\Delta\Omega$ as a function of the coupling parameter r at fixed $\alpha = 0.9997$ and for $N = 380$ photons per time bin. Figure 7(a) shows the absolute 3σ noise in wavelength units comparing classical WGM, classical WGM-MZI, and entangled WGM-MZI; (b) shows the noise ratio relative to the classical WGM-MZI case, i.e. the SNR enhancement factor.

Figure 8 shows the region (dark grey area) that is excluded when we require that the dynamic range of the entangled WGM-MZI measurement is greater than the 3σ value of the noise in the resonance position. The dynamic range is defined as the distance along the detuning axis of the spectrum from the maximum gradient point where we perform the measurement to the nearest stationary point in the spectrum. That is, if the resonance position moves more than the dynamic range, the sign of the transmission spectrum gradient changes and we can no longer reliably read-off the resonance position from the transmission intensity. The light grey areas in Figure 8 show regions where the noise for the entangled WGM-MZI case is 20%, 40%, 60%, and 80% of the dynamic range.

From Figure 8 we see that the most robust SNR enhancement is obtained in the overcoupling regime. The dynamic range condition also rules out the large SNR en-

hancements predicted near critical coupling, as did considering the spectral width of the input photons in the

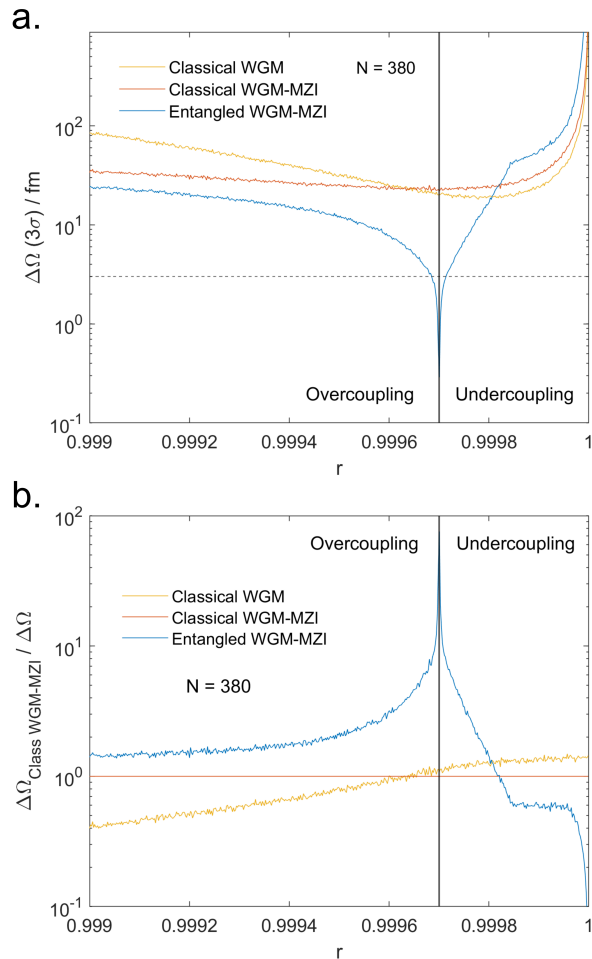


FIG. 7. Noise in WGM wavelength shift for all three measurement cases. (a) Noise (3σ) in the WGM wavelength shift against r at fixed photon number per time bin $N = 380$ and $\alpha = 0.9997$. (b) SNR enhancement factor for WGM wavelength shift relative to classical WGM-MZI case.

main text. The limits on r will be determined by experimental constraints. The optimum SNR enhancement is a trade-off between having noise much lower than the dynamic range for a more overcoupled resonator, and higher SNR enhancement closer to critical coupling.

Figure 9 compares the limits on SNR enhancement due to dynamic range to the limits due to the input photon spectral width (plotted in Figure 5 in the main text). The factor of 4 SNR enhancement at linewidth ratio 0.1 is still achieved with values of r for which the 3σ noise level is 40-60% of the dynamic range for the entangled WGM-MZI measurement. If we allow the photon spectral width to be arbitrarily narrow we see that in principle a factor of 10 enhancement in the SNR is possible when the 3σ noise level is 60-80% of the dynamic range.

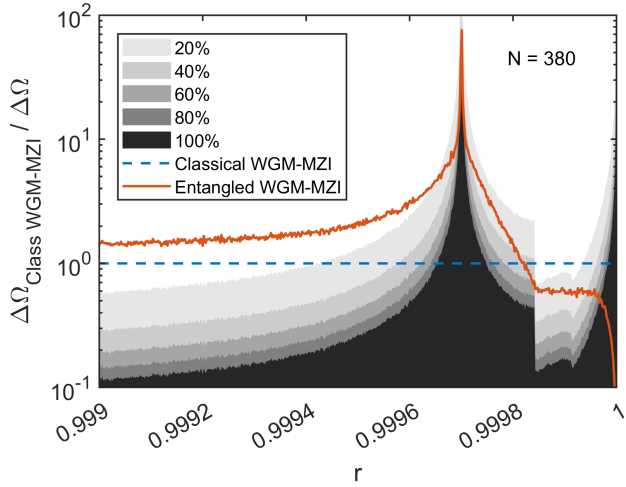


FIG. 8. Range of robust SNR enhancement allowed by dynamic range. SNR enhancement factor for WGM wavelength shift relative to classical WGM-MZI case plotted for the entangled WGM-MZI case (orange line) at fixed photon number per time bin $N = 380$ and $\alpha = 0.9997$. The grey areas are excluded when we require that the 3σ value of the entangled WGM-MZI noise is less than a percentage of the dynamic range for the measurement.

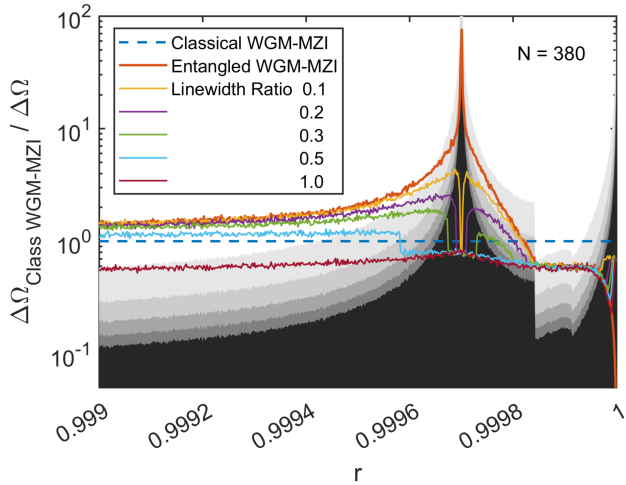


FIG. 9. Comparison between limits due to dynamic range and input photon spectral width. Dynamic range is plotted as in Figure 8 along with the input linewidth comparison from Figure 5 in the main text. Linewidth ratio is the ratio between the input photon spectral width and the classical WGM linewidth.